Realization of photonic p-orbital higher-order topological insulators

Zhang, Yahui; Bongiovanni, Domenico; Wang, Ziteng Wang; Xia, Shiqi; Hu, Zhichan; Song, Daohong; Jukić, Dario; Xu, Jingjun; Morandotti, Roberto; Buljan, Hrvoje; ...

Download date / Datum preuzimanja: **2024-12-24**

LETTER

Realization of photonic *p*-orbital higher-order topological insulators

Yahui Zhang[1†], Domenico Bongiovanni[1,2†], Ziteng Wang[1†], Xiangdong Wang[1†], Shiqi Xia[1], Zhichan Hu[1], Daohong Song[1,3], Dario Jukić[4], Jingjun Xu[1], Roberto Morandotti[2], Hrvoje Buljan[1,5*] and Zhigang Chen[1,3*]

Abstract

The orbital degrees of freedom play a pivotal role in understanding fundamental phenomena in solid-state materials as well as exotic quantum states of matter including orbital superfluidity and topological semimetals. Despite tremendous efforts in engineering synthetic cold-atom, as well as electronic and photonic lattices to explore orbital physics, thus far high orbitals in an important class of materials, namely, higher-order topological insulators (HOTIs), have not been realized. Here, we demonstrate *p*-orbital corner states in a photonic HOTI, unveiling their underlying topological invariant, symmetry protection, and nonlinearity-induced dynamical rotation. In a Kagome-type HOTI, we find that the topological protection of *p*-orbital corner states demands an orbital-hopping symmetry in addition to generalized chiral symmetry. Due to orbital hybridization, nontrivial topology of the *p*-orbital HOTI is "hidden" if bulk polarization is used as the topological invariant, but well manifested by the generalized winding number. Our work opens a pathway for the exploration of intriguing orbital phenomena mediated by higher-band topology applicable to a broad spectrum of systems.

Keywords Higher-band topology, Orbital degrees of freedom, Generalized chiral symmetry, Bulk polarization, Winding number, Breathing Kagome lattice

†Yahui Zhang, Domenico Bongiovanni, Ziteng Wang and Xiangdong Wang contributed equally to this work

*Correspondence:
Hrvoje Buljan
hbuljan@phy.hr
Zhigang Chen
zgchen@nankai.edu.cn
[1] The MOE Key Laboratory of Weak-Light Nonlinear Photonics, TEDA Applied Physics Institute and School of Physics, Nankai University, Tianjin 300457, China
[2] INRS-EMT, 1650 Blvd. Lionel-Boulet, Varennes, QC J3X 1S2, Canada
[3] Collaborative Innovation Center of Extreme Optics, Shanxi University, Taiyuan 030006, Shanxi, China
[4] Faculty of Civil Engineering, University of Zagreb, A. Kačića Miošića 26, 10000 Zagreb, Croatia
[5] Department of Physics, Faculty of Science, University of Zagreb, Bijenička C. 32, 10000 Zagreb, Croatia

In condensed matter systems, an important characteristic of electrons besides charge and spin is the orbital degree of freedom (ODoF), which plays a crucial role in understanding unconventional properties in solid-state materials as well as in "orbital physics" toward unveiling the science and technology of correlated electrons [1]. However, due to the complexity and various degrees of freedom simultaneously involved in real materials, it has always been a challenge to fully unravel the physics of strongly correlated electronic matter mediated by the ODoF via controlled experiments. On the other hand, the interest in synthetic orbital systems including trapped atoms in optical lattices surged rapidly over the past decade [2, 3], leading to "orbital-only" quantum emulators not only for fermions but also for bosons. For example, orbital lattices have been employed to demonstrate complex Bose–Einstein condensates and orbital superfluidity [4] as well as exotic topological semimetal phases [5]. Clearly, the capability of purposely preparing atoms to higher orbital

bands in optical lattices has opened the door for understanding orbital physics in condensed matter systems, with the ultimate goal of exploring new quantum states of matter not found in natural solids.

Apart from ultracold atoms in optical lattices, other synthetic platforms wherein the ODoF has emerged and caught increasing attention include semiconductor polaritonic lattices [6, 7], laser-written photonic lattices [8, 9], nanomechanical resonant structures [10], and atom-to-atom engineered electronic lattices [11, 12]. In particular, by employing the *p*-orbital bands of polariton micropillars arranged in a honeycomb lattice, both orbital edge states and exotic Dirac dispersions were observed [13, 14]. These artificial lattices can be used to flexibly manipulate orbital Dirac matter with transport properties and topological features difficult to achieve in conventional solid-state systems.

Using such synthetic lattice platforms, symmetry-protected topological (SPT) phases have been extensively explored due to their peculiar characteristics and unique potential applications associated with robust boundary states, especially in photonics [15–18]. Notable recent endeavors have focused on the realization of higher-order topological insulators (HOTIs) [19–25]—a new class of topological materials that do not obey the conventional bulk-edge correspondence principle [18, 26, 27]. While their underlying physics is still an ongoing subject of investigation, higher-order topological corner states have been extensively tested for various applications, including topological nanocavities and lasers [28–30]. However, to date, all experimental studies in HOTI systems relied on the *s*-orbital band, leaving higher-orbital HOTIs unexplored except for a recent proposal [31]. As a popular model of HOTIs, the breathing Kagome lattices (BKLs) exhibiting C_3 rotational symmetry have been widely explored for demonstration of HOTIs in many different systems [32–41]. Although there is a continuing debate concerning the HOTI classification for the BKLs [42], experiments using metamaterials have unambiguously identified the higher-order topology for the *s*-orbital BKL-type topological crystalline insulators [39]. Furthermore, their robustness to symmetry-breaking perturbations has also been validated [41]. It is thus natural to ask: can we realize an HOTI manifesting higher orbitals using a synthetic BKL platform, and what are the distinctive topological features and new perspectives associated with the orbital HOTIs?

In this work, we experimentally demonstrate *p*-orbital HOTIs using photonic BKLs established by a continuous-wave (CW) laser-writing technique. In a triangle-shaped nontrivial BKL, both p_x- and p_y-type orbital corner states are observed, with characteristic intensity and phase structures manifesting the zero-dimensional

"zero-energy" modes. Furthermore, corner excitation leads to dynamical rotation of a dipole beam due to the nonlinearity-induced lifting of p_x and p_y orbital mode degeneracy. We calculate the band structures and topological invariants of the orbital HOTIs and confirm their nontrivial topology from the winding number, albeit the topology is "hidden" in the conventional bulk polarization due to orbital coupling-induced band crossing. The SPT phase of orbital HOTIs is found to be inherited from the lower *s*-band Hamiltonian, being protected by the C_3 rotational symmetry, the generalized chiral symmetry (GCS), as well as by a previously unknown orbital-hopping symmetry not applicable to the *s*-band HOTIs.

The photonic BKL platform used to demonstrate *p*-orbital HOTIs is illustrated in Fig. 1a, which has six-unit cells comprised of three sublattices (A, B, and C) with intracell and intercell hopping amplitudes t_1 and t_2, respectively. When $t_1 < t_2$, the BKL exhibits a nontrivial topology, featuring SPT corner states as in previously studied *s*-orbital HOTIs [32–35]. In our laser-written BKL, t_1 and t_2 are tuned through the respective waveguide distances, while every waveguide supports two dipole modes (see left inset, Fig. 1a), allowing for both p_x and p_y orbitals. When the ODoF is taken into account, additional hopping amplitudes $t_\sigma(t_\pi)$ must be considered, being those responsible for the longitudinal (transverse) hopping when the *p*-orbitals are oriented parallel (perpendicular) to the bond direction [43] (see right inset, Fig. 1a). Under the tight-binding model, the full energy spectrum is calculated from the *p*-band Hamiltonian [31] (see "Methods") and plotted in Fig. 1b, where localized orbital corner states in the strongly topologically nontrivial regime are marked. Although the nontrivial phase occurs once $t_1 < t_2$ in an infinite BKL, we found that localized corner states are present in a narrower window of parameters in an experimentally accessible BKL. Furthermore, the band structure for a representative nontrivial case is plotted in Fig. 1c, which displays six topological orbital corner modes in the bandgap with eigenvalues close to zero. Two typical corner modes exhibiting characteristic p_x- and p_y-type orbitals are shown in Fig. 1d1, d2: their amplitudes distribute equally among three corner sites, showing no leaking to the nearest-neighbor sites but only a weak amplitude in the next-nearest-neighbor (NNN) sites. If we consider, for example, the p_x-type orbital at the top vertex, the corner mode is exponentially localized at the A-sublattice sites with an opposite phase between the dipoles in the corner and the two NNN sites (Fig. 1d1)—a characteristic feature of the HOTI corner modes [34, 44]. Other orbital orientations with unequal amplitude distributions at three vertices of a finite-sized BKL are discussed in the Additional file 1. Here we point out the difference
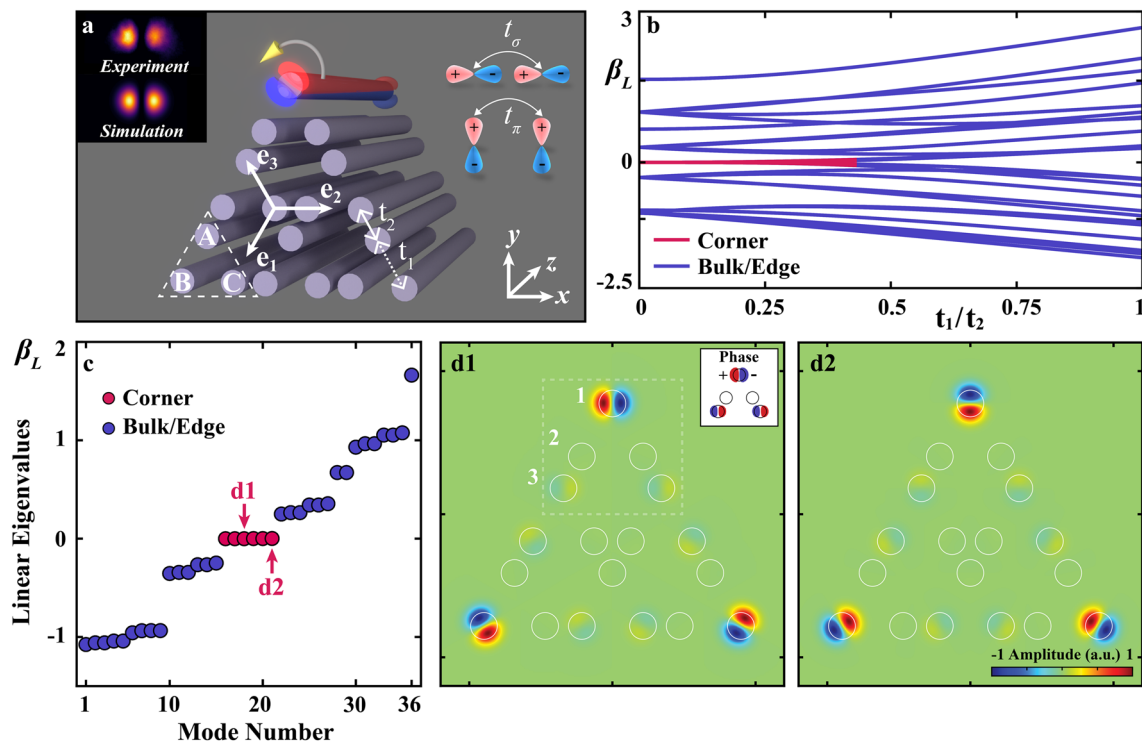
Fig. 1 Illustration of "zero-energy" *p*-orbital topological corner states in a BKL. **a** Schematic diagram of the triangular BKL with six-unit cells, where the white dashed triangle marks one unit cell consisting of three sublattices (A, B, and C), and t_1 and t_2 indicate the intracell and intercell hopping amplitudes, respectively. Each lattice site corresponds to a laser-written waveguide, which supports *p*-orbital modes (see the left inset). Two types of orbital hopping amplitudes, t_σ and t_π, are illustrated in the right inset. In the top vertex of the lattice, we depict the rotation of an orbital corner state under nonlinear excitation. **b** Calculated eigenvalue spectrum β_L as a function of t_1/t_2 at $t_\pi/t_\sigma = -0.3$ for the finite-size BKL shown in (**a**), where distinct "zero-energy" corner states in the highly nontrivial regime are marked in red. **c** Calculated band structure for the BKL with $t_1/t_2 = 0.1$, showing six corner states (red dots) at $\beta_L \approx 0$, where two representatives (p_x- and p_y-type modes relative to the top corner) are plotted in (**d1**, **d2**). Note that a topological *p*-orbital corner mode, as the p_x-mode illustrated in (**d1**), is characteristically localized at the corner site 1, with a staggered phase distribution in the NNN site 3 but zero amplitude at the nearest-neighbor site 2

between the BKL employed in this work, where each constituting waveguide supports both fundamental and *p*-orbital modes, and the 2D Su–Schrieffer–Heeger (SSH) lattices used in previous work [44], where each waveguide supports a single mode and no *p*-orbitals were involved.

In our experiments, we write waveguides site-by-site in a nonlinear crystal [45], establishing both topologically nontrivial (Fig. 2a1) and trivial (Fig. 2a2) photonic BKLs. All waveguides remain intact during measurements, whereas probing of corner states is performed with an appropriately-shaped beam that can undergo linear or nonlinear propagation depending on whether a bias field is employed [44]. For a direct comparison of propagation through the 20-mm-long lattices, the amplitude and phase of the probe beam are pre-modulated to mimic the corner mode profiles in Fig. 1d (see Additional file 1). Measured results to illustrate orbital HOTI corner states are presented in Fig. 2b1–f2. Specifically, for the excitation of the p_x-type orbital corner states, the input probe beam is made of three *x*-oriented dipoles with a

nonuniform intensity distribution and staggered phase, i.e., $(0, \pi)$ for the top dipole vs. $(\pi, 0)$ for the other two (Fig. 2b1). The modulated probe beam is then launched into the BKLs at the top corner of the synthetic structure (the three uppermost A-sublattice sites). After linear propagation through the trivial and nontrivial BKLs, a significant difference is observed. In the nontrivial regime, the probe beam remains to be corner-localized in the A sublattice, with no intensity reaching the neighboring B and C sites (Fig. 2c1), thus confirming the formation of orbital HOTI corner states (see Fig. 1d1). On the contrary, the same probe beam becomes strongly distorted in the trivial regime, spreading into the edge and bulk sites with a tangible intensity distribution also in the B and C sites (Fig. 2c2). These results are corroborated by numerical simulations showing good agreement with the experiments (Fig. 2d1, d2).

In another set of measurements, the input probe beam is modulated so as to excite p_y-type orbital corner states, see Fig. 1d2. Similar results confirm the formation of a *p*
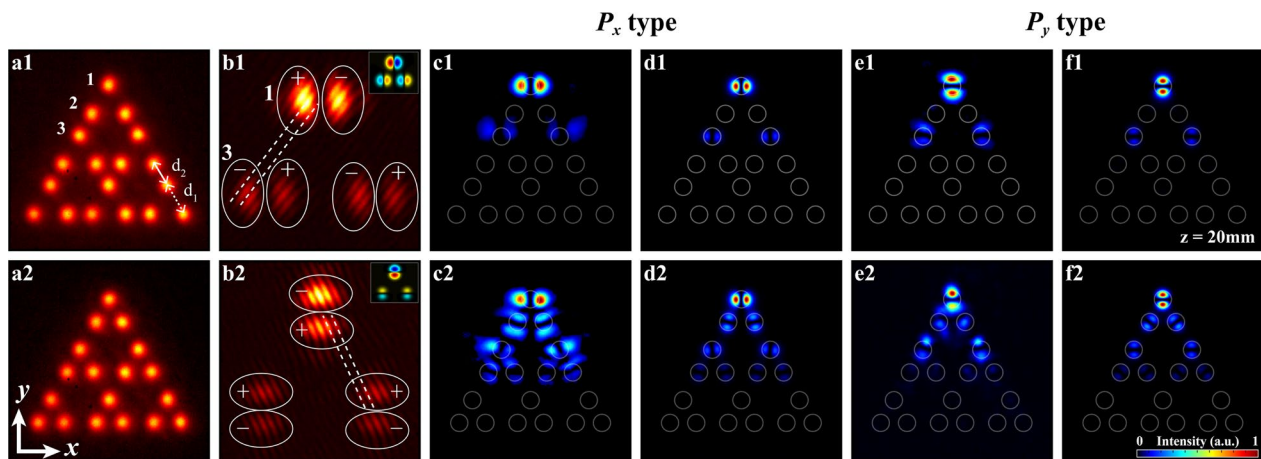
Fig. 2 Demonstration of *p*-orbital topological corner states in a photonic BKL. **a1**, **a2** Experimental BKLs in the nontrivial (**a1**) and trivial (**a2**) regimes. **b1**, **b2** Zoom-in interferograms of the probe beam with a reference plane wave, showing the out-of-phase relation between the corner site 1 and its NNN site 3 for both p_x- (**b1**) and p_y-type (**b2**) orbital excitations. The white ellipses identify the three-dipole probe beams, where the plus/minus signs represent $0/\pi$ phases for each dipole, and dashed straight lines are added to see the phase structure from the shifted (**b1**) and the aligned (**b2**) interference fringes, confirming the staggered phase structures (see also numerical results in right insets). **c1**, **c2** Observed output intensity patterns in nontrivial (**c1**) and trivial (**c2**) BKLs stemming from a p_x-orbital corner excitation. **d1**, **d2** Numerical simulations corresponding to (**c1**, **c2**). Results from a p_y-orbital corner excitation are shown in (**e1**, **e2**) and (**f1**, **f2**). Grey circles in (**c1**–**f2**) mark the BKL sites. Lattice parameters are $d_1 = 39\,\mu m$ and $d_2 = 31\,\mu m$ for *p*-orbital excitation in the nontrivial BKL. Note the zero amplitude at the nearest-neighbor site 2 in (**c1**–**f1**)

-orbital mode in the orthogonal direction (see Fig. 2b2 and Fig. 2e1–f2). In addition, to validate the need for the staggered phase structure, a series of experiments and numerical simulations are performed by setting the input dipoles all in phase for direct comparison (see Additional file 1). Our results reveal that both p_x- and p_y-type orbital corner states can be realized under appropriate excitations.

To demonstrate that the *p*-orbital BKL is indeed a symmetry-protected HOTI, we need to identify the topological invariant and prove the robustness of the corner states. The first candidate is the bulk polarization [46], or the Z_3 Berry phase [31, 47] of the *s*-band BKL. In Fig. 3a, b1, b2, we plot the calculated polarization and 6-band structures as a function of the coupling ratio t_π/t_σ. Polarizations of the upper three bands are always 0, 1/3, and 2/3, however the order of these three values changes with t_π/t_σ as shown in Fig. 3a. The sum of the quantized polarizations of the upper three bands is always 1, yet this value must be regarded as mod 1, which implies that polarization vanishes. Although the vanishing of bulk polarization happens only in a parameter region where one needs to consider three bands instead of two or five [31], it suggests that polarization is not a good topological invariant at least for the *p*-orbital BKL.

To resolve the above issue, we introduce an auxiliary Hamiltonian $H'(\boldsymbol{k}, \theta)$ obtained via a unitary transformation of the *p*-band Hamiltonian $H(\boldsymbol{k})$ [31, 47], which employs a rotational operator $R(\theta)$ (see "Methods" and

Additional file 1). The C_3 symmetry and the GCS are both preserved as θ is changed (see Additional file 1). At $\theta = 4\pi/3$, the auxiliary Hamiltonian is identical to the *p*-orbital BKL Hamiltonian, whereas at $\theta = 0$ it is composed of two independent BKL Hamiltonians—one for the t_σ hopping and the other for the t_π hopping, just as if we had two decoupled *s*-band BKLs (Fig. 3c). For each of these Hamiltonian components, the topological invariant is given by the bulk polarization [46], which depends solely on t_1/t_2. In Fig. 3d we plot the band-gap structure of the auxiliary Hamiltonian as a function of θ, showing that the gap does not close as θ is varied from 0 to $4\pi/3$. Thus, the key point is that the orbital BKL described by the auxiliary Hamiltonian does not undergo a topological phase transition, so the *p*-orbital Hamiltonian at $\theta = 4\pi/3$ is topologically non-trivial, just as for the *s*-band BKLs when $t_1/t_2 < 1$ (see Additional file 1 for details).

Another interesting question that arises is whether there is a topological invariant that can manifest the nontrivial topology for the orbital HOTIs directly. To this end, we propose a generalized winding number $\mathcal{W}$ as defined in "Methods" [14, 48]. Results are displayed in Fig. 3e: $\mathcal{W} = 2$ is found for the topologically nontrivial regime ($t_1/t_2 < 1$) and $\mathcal{W} = 0$ for the trivial regime $t_1/t_2 > 1$. We emphasize that $\mathcal{W}$ is clearly a good topological invariant, independent of θ. In fact, for BKL-like orbital HOTIs, the need of using the winding number $\mathcal{W}$ is essential. This is because, for the Kagome geometry,
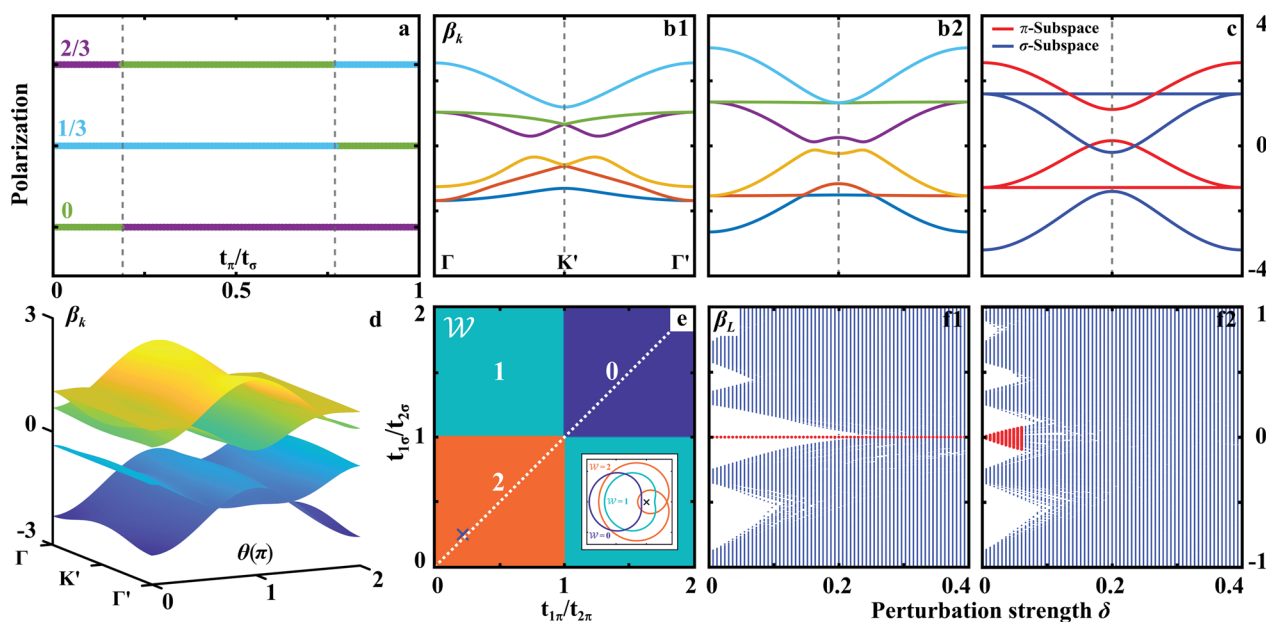
Fig. 3 Theoretical analysis of *p*-orbital HOTIs: topological invariant and corner-mode robustness. **a** Bulk polarization of the upper three bands (blue, green, and purple as plotted in (**b1**) and (**b2**)) as a function of the orbital coupling ratio t_π/t_σ, exhibiting step jumps at the band-crossing points (marked by vertical dashed lines). The sum of the quantized polarizations of the upper three bands is $(0 + 1/3 + 2/3) mod 1 = 0$. **b1**–**b2** Band structures plotted for (**b1**) $t_\pi/t_\sigma = -0.19$ and (**b2**) $t_\pi/t_\sigma = -0.77$ at $t_1/t_2 = 0.6$ and $\theta = 4\pi/3$, showing the change in band-crossing for the upper three bands. **c** Band structure of the auxiliary Hamiltonian $H'(\mathbf{k}, \theta)$ calculated for $t_1/t_2 = 0.6$ and $t_\pi/t_\sigma = -0.8$ at $\theta = 0$, which is equivalent to two sets of decoupled *s*-band BKLs: red for one set and dark blue for the other set. **d** 3D plot of the band structure of $H'(\mathbf{k}, \theta)$ as a function of θ, showing that the gap at zero energy remains open for any θ (or for that matter, any orbital hybridization). **e** Calculated winding numbers, where the white dotted line marks the orbital-hopping-symmetry condition $t_{1\sigma}/t_{2\sigma} = t_{1\pi}/t_{2\pi}$ required for topological protection of the orbital corner states. Here, circles in the lower inset illustrate distinct windings for each case, and the blue cross in the $\mathcal{W} = 2$ region corresponds to the experimental parameters used to realize the *p*-orbital HOTI. **f1**–**f2** Robustness test of orbital corner states in a rhombic BKL obtained by applying random perturbations with increasing strengths δ between site couplings that (**f1**) preserve the A-SubSy (i.e., without A-A coupling) and (**f2**) break the A-SubSy (i.e., with A-A coupling). The corner modes (red circles) remain at zero energy in (**f1**) but not in (**f2**). See Additional file 1 for details

one cannot physically decouple the system into two independent Hamiltonians—one for the t_σ and the other for the t_π hopping, akin to the chiral Hamiltonian for the quantum spin Hall effect [49, 50]. Orbital hybridization leads to band crossing and mixing from the σ and π subspaces as the parameter θ is changed, so one cannot relate a single band to a particular subspace. The vanishing bulk polarization cannot unequivocally reveal the underlying nontrivial topology in the BKL. This is quite different from the 2D SSH-based HOTIs [19, 22–24, 44, 51], which can be decomposed into two independent Hamiltonians associated with orthogonal orbital hopping (see, e.g. Ref [51].). Given that BKL-based HOTIs are protected by the GCS, the use of the winding number can resolve this issue. If θ changes progressively from 0 to $4\pi/3$, the band gap at zero-energy either remains open as shown in Fig. 3d or simply exhibits a "trivial" touching without band inversion—see Additional file 1. Consequently, the upper and lower three bands never topologically entangle. Since a continuous tuning of θ does not induce a phase transition, the topological invariants are entirely

inherited from the decoupled auxiliary Hamiltonian at $\theta = 0$.

The case for $\mathcal{W} = 1$ in Fig. 3e merits further discussion. Since the BKLs possess a C_3 symmetry, the winding numbers for each direction along the lattice unit vectors are identical (see "Methods"). $\mathcal{W} = 2$ implies that both subspaces of the auxiliary Hamiltonian at $\theta = 0$ are topologically nontrivial, thus there are two SPT states (corresponding to p_x- and p_y-orbitals) in each corner. In contrast, $\mathcal{W} = 1$ indicates that only one subspace is topologically nontrivial while the other is indeed trivial. Intuitively, one would think that half of the corner states should persist as θ is changed. However, as the trivial and nontrivial subspaces are coupled, the corner states of the whole system merge into the bulk. The absence of corner states for $\mathcal{W} = 1$ is in agreement with the condition $t_{1\sigma}/t_{2\sigma} = t_{1\pi}/t_{2\pi}$ that must be held in order to pin the orbital corner states at zero energy (see Additional file 1): the diagonal white line in Fig. 3e illustrating this condition does not cross the two $\mathcal{W} = 1$ quadrants. Thus, we only have topological corner states in the $\mathcal{W} = 2$ region.

To prove the immunity of an orbital corner state to perturbations, we investigate its robustness in a rhombic BKL, which hosts two orthogonal corner modes only at one corner, by following the approach recently developed for the study of sub-symmetry (SubSy)-protected topological states [41]. Here we assume that neglecting the long-range hopping is a reasonable approximation. Our results (Fig. 3f1, f2) show that orbital corner states residing in the A sublattice are protected under perturbations that respect the A-subsymmetry [41]. Moreover, we uncover that in addition to the C_3 symmetry and the GCS, the topological protection of the *p*-orbital HOTI corner states requires a counterintuitive *orbital-hopping symmetry* (see "Methods" and Additional file 1). Such a symmetry demands $t_{1\sigma}/t_{2\sigma} = t_{1\pi}/t_{2\pi}$ (marked by the white dashed line in Fig. 3e), which basically implies that the two orthogonal orbital hoppings should experience no difference when the lattice breathing characterized by t_1/t_2 occurs. The lattice used in our experiments satisfies this condition with good approximation, as indicated by the blue cross in the region of $\mathcal{W} = 2$ in Fig. 3e.

Finally, we observe an intriguing phenomenon—the dynamical rotation of orbital corner modes under the action of nonlinearity. As discussed in Additional file 1, the six *p*-orbital corner modes in a finite-size BKL are not all degenerate in their eigenvalues. Besides the two typical corner modes exhibiting characteristic—p_x- and p_y-type orbitals shown in Fig. 1d1, d2, the other four orbital corner-mode eigenvalues are degenerate

in pairs. This leads to mode beating, and the amplitude distribution and orbital orientation in the three corners are susceptible to parameter variation such as in lattice size or potential. In our experiment, when a dipole-like beam is initially tilted away from the "equilibrium" position of the p_x- or p_y-orbital mode, excitation at one corner leads to a dipole rotation towards the preferred orbital orientation under a self-focusing nonlinearity. A typical example is shown in Fig. 4, where both clockwise (Fig. 4a1–a4) and counter-clockwise (Fig. 4b1–b4) rotations of about 10° are observed when the top corner is excited with a dipole beam tilted, respectively, at $\theta = -30°$ and $\theta = 30°$ relative to the *y*-axis.

To better understand the underlying physical mechanism, we investigate numerically the observed phenomenon by use of the discrete NLSE for nonlinear beam propagation (see Additional file 1). We find that such rotations can be explained by the nonlinearity-induced lifting of the orbital mode degeneracy (Fig. 4c) since an oblique *p*-orbital can be regarded as the superposition of p_x- and p_y-type orbital components. Nonlinearity can introduce local variation of the lattice potential and break the lattice symmetry, and depending on the strength, it can also drive the corner modes away from zero-energy position and even form corner solitons [44]. Here we use a weak self-focusing nonlinearity as encountered in the experiment, and numerically show that the dynamical rotation can be explained by a dissimilar response of two orthogonal
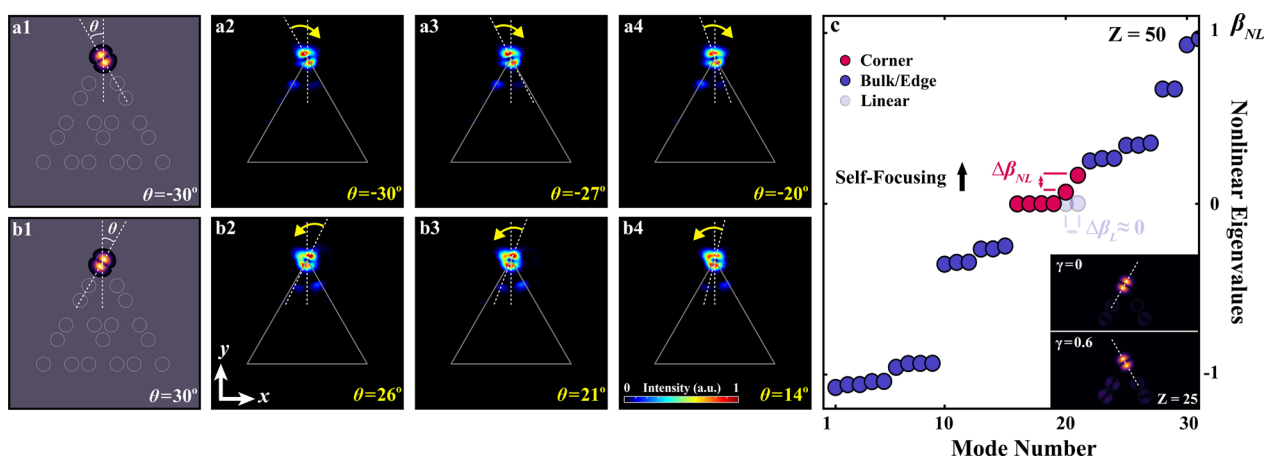

Fig. 4 Nonlinearity-induced dynamical rotation of *p*-orbital corner states. **a1**, **b1** Excitation of the top corner of a nontrivial BKL with a dipole-like beam initially tilted at (**a1**) $\theta = -30°$ and (**b1**) $\theta = 30°$ with respect to the *y*-axis. **a2**–**a4** Experimental output of the orbital corner state under an initial excitation corresponding to (**a1**), showing a clockwise rotation under the action of a self-focusing nonlinearity (with a bias field of 175 kV/m). **b2**–**b4** Opposite rotation observed under the same nonlinearity when the initial excitation corresponds to (**b1**). The grey triangle in each panel outlines the BKL boundaries. Note that no rotation occurs when the dipole is initially oriented along the *y*-axis. **c** Orbital band structure calculated from the discrete NLSE at a dimensionless distance $Z = 50$, for a probe beam incident at $\theta = 30°$ and propagating under both linear ($\gamma = 0$) and nonlinear ($\gamma = 0.6$) regimes. A tilted dipole-like beam excites two orthogonal orbital corner modes which are nearly degenerate in the linear regime ($\Delta\beta_L \approx 0$). Here, the nonlinearity lifts the degeneracy and increases the difference $\Delta\beta_{NL}$ between the nonlinear eigenvalues, in turn leading to a rotation of the orbital state. Insets illustrate the orientation of a probe beam at $Z = 25$ in the two regimes

components to the action of nonlinearity, which lifts the degeneracy of the two orbital modes.

Before closing, we further emphasize the following differences between this work and that in Ref. [40], which also used a BKL-type lattice but focused on nonlinear *s*-orbital HOTI. (1) The ODoF requires each waveguide in the BKL can support at least the higher orbital *p*-mode, while the fs-laser-writing BKL waveguide as used for the *s*-orbital HOTI typically supports only a fundamental *s*-mode. (2) Different from the *s*-orbital, the coupling strength of the *p*-orbital is orientation-dependent, so one needs two coupling t_π and t_σ to describe the orbital coupling dynamics. (3) For the *s*-orbital HOTI, the conventional bulk polarization can be used to characterize the topological properties of the corner states as in Ref. [40]. However, we have shown that the nontrivial topology of the *p*-orbital HOTI is "hidden" if the bulk polarization is used due to hybridization effects, but well manifested by the generalized winding number (see also discussion in Section IX of the Additional file 1). (4) We have found that the topological protection of *p*-orbital corner states demands an orbital-hopping symmetry, which has no counterpart whatsoever in the *s*-orbital HOTI. (5) Apart from different mechanisms for the employed nonlinearity itself, Ref [40] focused on nonlinear HOTI corner states and corner solitons, while the nonlinearity in our current work is used as "perturbation" to induce *p*-orbital corner mode rotation which is not applicable to the *s*-orbital HOTI.

We have thus shown that *p*-orbital HOTIs in photonic BKLs have a nontrivial band topology inherited from their *s*-orbital counterparts, which is characterized by the winding number rather than the quantized bulk polarization. Higher-order orbital corner states are topologically protected by the GCS along with an orbital-hopping symmetry not found in HOTIs where σ- and π-orbital couplings can be fully decoupled. These results have a direct impact on topological photonics involving the ODoF, especially given that different experimental platforms have enabled active and precise control of gain and loss, on-site energy, and coupling strength, in both real and synthetic dimensions [52–58]. For instance, using the ODoF, it is possible to construct a host of new topological phases

including hybrid quadrupole topological insulators [59] and orbital modes in non-Euclidean surfaces with disclinations [60]. Our results may prove relevant to those studies, as well as to the development of new photonic devices such as topological vortex waveguides and topological lasers.

1 Methods
1.1 Orbital Hamiltonian and the winding number
Under the tight-binding approximation, the *p*-orbital corner states in a BKL can be found from the real-space Hamiltonian *H* expressed as [31]:

$$H = \sum_{m,n} t_{1\sigma}\left(a_{1_{m,n}}^\dagger b_{1m,n} + b_{2_{m,n}}^\dagger c_{2m,n} + c_{3_{m,n}}^\dagger a_{3m,n}\right) + \sum_{m,n} t_{2\sigma}\left(a_{1_{m,n}}^\dagger b_{1m+1,n} + b_{2_{m,n}}^\dagger c_{2m-1,n+1} + c_{3_{m,n}}^\dagger a_{3m,n+1}\right)$$
$$+ \sum_{m,n} t_{1\pi}\left(\widetilde{a}_{1_{m,n}}^\dagger \widetilde{b}_{1m,n} + \widetilde{b}_{2_{m,n}}^\dagger \widetilde{c}_{2m,n} + \widetilde{c}_{3_{m,n}}^\dagger \widetilde{a}_{3m,n}\right) + \sum_{m,n} t_{2\pi}\left(\widetilde{a}_{1_{m,n}}^\dagger \widetilde{b}_{1m+1,n} + \widetilde{b}_{2_{m,n}}^\dagger \widetilde{c}_{2m-1,n+1} + \widetilde{c}_{3_{m,n}}^\dagger \widetilde{a}_{3m,n+1}\right) + h.c., \tag{1}$$

where $a_{i_{m,n}}(\widetilde{a}_{i_{m,n}})$, $b_{i_{m,n}}(\widetilde{b}_{i_{m,n}})$ and $c_{i_{m,n}}(\widetilde{c}_{i_{m,n}})$ $(i=1,2,3)$ are the σ-type (π-type) annihilation operators at the A, B, and C sublattice sites in the (m,n) th unit cell, directed along the primitive lattice vectors e_i. The coefficients $t_{1\sigma}(t_{2\sigma})$ and $t_{1\pi}(t_{2\pi})$ are the intracell (intercell) orbital coupling strengths (see Fig. 1a; Additional file 1). In Fig. 1, the linear band structure (β_L) is obtained by diagonalizing *H* for different dimerization parameters t_1/t_2 under an orbital hopping symmetry $t_{1\sigma}/t_{2\sigma} = t_{1\pi}/t_{2\pi}$. The *p*-orbital mode distribution is found by retrieving both p_x- and p_y-components from the calculated eigenvectors of *H*. In the momentum space, the Fourier transform of *H* for an orthogonal basis along *x*- and *y*-directions reads as

$$H(\boldsymbol{k}) = \begin{pmatrix} 0 & H_1^\dagger & H_3 \\ H_1 & 0 & H_2^\dagger \\ H_3^\dagger & H_2 & 0 \end{pmatrix}, \tag{2}$$

where the matrix entries H_i $(i=1,2,3)$ are 2×2 matrices defined as $H_i(\boldsymbol{k}) = \boldsymbol{e}_i\boldsymbol{e}_i^\dagger\left(t_{1\sigma} + t_{2\sigma}e^{i\boldsymbol{k}\cdot\boldsymbol{e}_i}\right) + \boldsymbol{d}_i\boldsymbol{d}_i^\dagger\left(t_{1\pi} + t_{2\pi}e^{i\boldsymbol{k}\cdot\boldsymbol{e}_i}\right)$, with $\boldsymbol{k} = (k_x, k_y)$ being the transverse wave vector, and $\boldsymbol{d}_i$ the unit vector orthogonal to $\boldsymbol{e}_i$. The SPT phase of the *p*-band BKL model is identified from an auxiliary Hamiltonian $H'(\boldsymbol{k}, \theta)$, which is achieved by applying a unitary transformation on $H(\boldsymbol{k})$ (see Additional file 1 for details). The structure of $H'(\boldsymbol{k}, \theta)$ is identical to that in Eq. (2), with the matrix entries $H_i(\boldsymbol{k})$ replaced by $H_i'(\boldsymbol{k}, \theta) = \begin{pmatrix} t_{1\sigma} + t_{2\sigma}e^{i\boldsymbol{k}\cdot\boldsymbol{e}_i} & 0 \\ 0 & t_{1\pi} + t_{2\pi}e^{i\boldsymbol{k}\cdot\boldsymbol{e}_i} \end{pmatrix}R(\theta)$, where $R(\theta) = \begin{pmatrix} \cos\theta & -\sin\theta \\ \sin\theta & \cos\theta \end{pmatrix}$ is the rotation operator. The orbital Kagome Hamiltonian $H(\boldsymbol{k})$ (Eq. 2) is fully equivalent to $H'(\boldsymbol{k}, \theta = 4\pi/3)$, i.e., at $\theta = 4\pi/3$. In our analysis, $R(\theta)$ is used to artificially tune the auxiliary Hamiltonian

$H'(\boldsymbol{k}, \theta)$ from the orbital-decoupled $\theta = 0$ to the physical $\theta = 4\pi/3$ Kagome model, to unequivocally identify the topological phase.

The winding number coefficients $\mathcal{W}_i$ are calculated from the matrix elements of $H'(\boldsymbol{k}, \theta)$ along each direction pointed by $\boldsymbol{e_i}$ in the first Brillouin zone through the following expression:

$$\mathcal{W}_i = \frac{1}{2\pi} \int_0^{2\pi} dk_i \frac{d\Phi_i(k_i)}{dk_i}, \quad i = 1, 2, 3 \tag{3}$$

with $\det\left[H'_i(\boldsymbol{k}, \theta)\right] = \left|\det\left[H'_i(\boldsymbol{k}, \theta)\right]\right| e^{i\Phi_i(\boldsymbol{k}, \theta)}$, where $\Phi_i(\boldsymbol{k}, \theta)$ is the argument of $\det\left[H'_i(\boldsymbol{k}, \theta)\right]$, and k_i is the wave vector along the direction $\boldsymbol{e_i}$. In general, for an arbitrary value of θ, we have $\mathcal{W} = \mathcal{W}_1 = \mathcal{W}_2 = \mathcal{W}_3$, i.e., all $\mathcal{W}_i$ are equal as long as the C_3 symmetry is preserved in the system.

1.2 Continuous model and numerical simulations

To provide a direct correspondence to the experimental results in our photonic platform based on a saturable photorefractive (PR) crystal (SBN:61), numerical simulations from the following continuous-model nonlinear Schrödinger-like equation (NLSE) are compared to the measurements [44]:

$$i\frac{\partial \Psi}{\partial z} = -\frac{1}{2k}\nabla_\perp^2 \Psi - \frac{k\Delta n}{n_0} \frac{\Psi}{1 + I_L(x, y) + I_P(x, y)}. \tag{4}$$

Here, $\Psi(x, y, z)$ is the electric field envelope, where x and y are the transverse coordinates and z is the propagation distance. $k = 2\pi n_0/\lambda_0$ is the wavenumber in the medium, where $n_0 = 2.35$ is the crystal refractive index and $\lambda_0 = 532$ nm is the laser wavelength. Δn is the refractive index change determined by both the crystal electrooptic coefficient and the bias field. $I_L(x, y)$ and $I_P(x, y)$ are the intensity patterns of the lattice-writing and probing beams, respectively. The strength of the nonlinearity is controlled by the probe-beam intensity and the bias field [44]. Solutions to Eq. (4) for orbital corner states in both trivial and nontrivial BKL geometries are found via the split-step Fourier transform method.

2 Experimental method

Experimental BKLs in trivial and nontrivial geometries are established by a site-to-site writing process of each component waveguide using an ordinarily-polarized CW green laser beam [45]. To attain a variable planar distribution, a spatial light modulator (SLM) is employed to modulate the initial phase of the laser beam in the Fourier space. The effective PR "memory effect" guarantees that all waveguides remain intact during the measurement time window. The excitation of the orbital corner states

is carried out with a low-power extraordinarily-polarized probe beam, which undergoes linear propagation through the lattices for the results presented in Fig. 2. The probe beam is appropriately shaped via amplitude and phase modulation in order to excite the *p*-orbital corner modes (see Additional file 1). In the nonlinear regime, a tilted dipole-like probe beam is launched at the top corner of the nontrivial BKL, where the strength of the self-focusing nonlinearity can be controlled by the probe-beam intensity and the bias field.

Availability of data and materials

Data supporting this manuscript are available upon request.

Declarations

Ethics approval and consent to participate

Not applicable.

Consent for publication

Not applicable.

References
1. Y. Tokura, N. Nagaosa, Orbital physics in transition-metal oxides. Science **288**, 462–468 (2000)
2. M. Lewenstein, W.V. Liu, Orbital dance. Nat. Phys. **7**, 101–103 (2011)
3. X. Li, W.V. Liu, Physics of higher orbital bands in optical lattices: a review. Rep. Prog. Phys. **79**, 116401 (2016)

4.   G. Wirth, M. Ölschläger, A. Hemmerich, Evidence for orbital superfluidity in the p-band of a bipartite optical square lattice. Nat. Phys. **7**, 147–153 (2010)

5.   K. Sun et al., Topological semimetal in a fermionic optical lattice. Nat. Phys. **8**, 67–70 (2011)

6.   T. Jacqmin et al., Direct observation of Dirac cones and a flatband in a honeycomb lattice for polaritons. Phys. Rev. Lett. **112**, 116402 (2014)

7.   P. St-Jean et al., Lasing in topological edge states of a one-dimensional lattice. Nat. Photon. **11**, 651–656 (2017)

8.   G. Cáceres-Aravena, L.E.F.F. Torres, R.A. Vicencio, Topological and flat-band states induced by hybridized linear interactions in one-dimensional photonic lattices. Phys. Rev. A **102**, 023505 (2020)

9.   D. Guzman-Silva, G. Caceres-Aravena, R.A. Vicencio, Experimental observation of interorbital coupling. Phys. Rev. Lett. **127**, 066601 (2021)

10.   J. Ma et al., Nanomechanical topological insulators with an auxiliary orbital degree of freedom. Nat. Nanotechnol. **16**, 576–583 (2021)

11.   M.R. Slot et al., Experimental realization and characterization of an electronic Lieb lattice. Nat. Phys. **13**, 672–676 (2017)

12.   M.R. Slot et al., P-Band engineering in artificial electronic lattices. Phys. Rev. X **9**, 011009 (2019)

13.   M. Milićević et al., Type-III and tilted Dirac cones emerging from flat bands in photonic orbital graphene. Phys. Rev. X **9**, 031010 (2019)

14.   M. Milićević et al., Orbital edge states in a photonic honeycomb lattice. Phys. Rev. Lett. **118**, 107403 (2017)

15.   M.C. Rechtsman et al., Photonic floquet topological insulators. Nature **496**, 196–200 (2013)

16.   M. Hafezi et al., Imaging topological edge states in silicon photonics. Nat. Photon. **7**, 1001–1005 (2013)

17.   A.B. Khanikaev et al., Photonic topological insulators. Nat. Mater. **12**, 233–239 (2013)

18.   T. Ozawa et al., Topological photonics. Rev. Mod. Phys. **91**, 015006 (2019)

19.   W.A. Benalcazar, B.A. Bernevig, T.L. Hughes, Quantized electric multipole insulators. Science **357**, 61–66 (2017)

20.   Z. Song, Z. Fang, C. Fang, (D-2)-dimensional edge states of rotation symmetry protected topological states. Phys. Rev. Lett. **119**, 246402 (2017)

21.   F. Schindler et al., Higher-order topological insulators. Sci. Adv. **4**, 0346 (2018)

22.   M. Serra-Garcia et al., Observation of a phononic quadrupole topological insulator. Nature **555**, 342–345 (2018)

23.   C.W. Peterson et al., A quantized microwave quadrupole insulator with topologically protected corner states. Nature **555**, 346–350 (2018)

24.   S. Imhof et al., Topolectrical-circuit realization of topological corner modes. Nat. Phys. **14**, 925–929 (2018)

25.   Y. Qi et al., Acoustic realization of quadrupole topological insulators. Phys. Rev. Lett. **124**, 206601 (2020)

26.   M. Kim, Z. Jacob, J. Rho, Recent advances in 2D, 3D and higher-order topological photonics. Light Sci. Appl. **9**, 130 (2020)

27.   B. Xie et al., Higher-order band topology. Nat. Rev. Phys. **3**, 520–532 (2021)

28.   Y. Ota et al., Photonic crystal nanocavity based on a topological corner state. Optica **6**, 786–789 (2019)

29.   W. Zhang et al., Low-threshold topological nanolasers based on the second-order corner state. Light Sci. Appl. **9**, 109 (2020)

30.   H.R. Kim et al., Multipolar lasing modes from topological corner states. Nat. Commun. **11**, 5758 (2020)

31.   X. Lu, Y. Chen, H. Chen, Orbital corner states on breathing Kagome lattices. Phys. Rev. B **101**, 195143 (2020)

32.   M. Ezawa, Higher-order topological insulators and semimetals on the breathing Kagome and pyrochlore lattices. Phys. Rev. Lett. **120**, 026801 (2018)

33.   A. El Hassan et al., Corner states of light in photonic waveguides. Nat. Photon. **13**, 697–700 (2019)

34.   X. Ni et al., Observation of higher-order topological acoustic states protected by generalized chiral symmetry. Nat. Mater. **18**, 113–120 (2019)

35.   H. Xue et al., Acoustic higher-order topological insulator on a Kagome lattice. Nat. Mater. **18**, 108–112 (2019)

36.   M. Ezawa, Higher-order topological electric circuits and topological corner resonance on the breathing Kagome and pyrochlore lattices. Phys. Rev. B **98**, 201402(R) (2018)

37.   S.N. Kempkes et al., Robust zero-energy modes in an electronic higher-order topological insulator. Nat. Mater. **18**, 1292–1297 (2019)

38.   M. Li et al., Higher-order topological states in photonic Kagome crystals with long-range interactions. Nat. Photon. **14**, 89–94 (2019)

39.   W. Peterson Christopher et al., A fractional corner anomaly reveals higher-order topology. Science **368**, 1114–1118 (2020)

40.   M.S. Kirsch et al., Nonlinear second-order photonic topological insulators. Nat. Phys. **17**, 995–1000 (2021)

41.   Z. Wang et al. Sub-symmetry protected topological states. arXiv:2205.07285 [physics.optics] (2022).

42.   M. Jung, Y. Yu, G. Shvets, Exact higher-order bulk-boundary correspondence of corner-localized states. Phys. Rev. B **104**, 195437 (2021)

43.   W.V. Liu, C. Wu, Atomic matter of nonzero-momentum bose-einstein condensation and orbital current order. Phys. Rev. A **74**, 013607 (2006)

44.   Z. Hu et al., Nonlinear control of photonic higher-order topological bound states in the continuum. Light Sci. Appl. **10**, 164 (2021)

45.   S. Xia et al., Unconventional flatband line states in photonic Lieb lattices. Phys. Rev. Lett. **121**, 263902 (2018)

46.   W.A. Benalcazar, T. Li, T.L. Hughes, Quantization of fractional corner charge in C_n-symmetric higher-order topological crystalline insulators. Phys. Rev. B **99**, 245151 (2019)

47.   H. Wakao et al., Higher-order topological phases in a spring-mass model on a breathing Kagome lattice. Phys. Rev. B **101**, 094107 (2020)

48.   C.L. Kane, T.C. Lubensky, Topological boundary modes in isostatic lattices. Nat. Phys. **10**, 39–45 (2013)

49.   M.Z. Hasan, C.L. Kane, Colloquium: topological insulators. Rev. Mod. Phys. **82**, 3045–3067 (2010)

50.   X.-L. Qi, S.-C. Zhang, Topological insulators and superconductors. Rev. Mod. Phys. **83**, 1057–1110 (2011)

51.   G. Pelegrí et al., Second-order topological corner states with ultracold atoms carrying orbital angular momentum in optical lattices. Phys. Rev. B **100**, 205109 (2019)

52.   S. Xia et al., Nonlinear tuning of PT symmetry and non-hermitian topological states. Science **372**, 72–76 (2021)

53.   N. Pernet et al., Gap solitons in a one-dimensional driven-dissipative topological lattice. Nat. Phys. **18**, 678–684 (2022)

54.   H. Pourbeyram et al., Direct observations of thermalization to a Rayleigh-Jeans distribution in multimode optical fibres. Nat. Phys. **18**, 685–690 (2022)

55.   C. Leefmans et al., Topological dissipation in a time-multiplexed photonic resonator network. Nat. Phys. **18**, 442–449 (2022)

56.   L. Yuan et al., Synthetic dimension in photonics. Optica **5**, 1396–1405 (2018)

57.   T. Ozawa, H.M. Price, Topological quantum matter in synthetic dimensions. Nat. Rev. Phys. **1**, 349–357 (2019)

58.   E. Lustig, M. Segev, Topological photonics in synthetic dimensions. Adv. Opt. Photon. **13**, 426–461 (2021)

59.   J. Schulz et al., Photonic quadrupole topological insulator using orbital-induced synthetic flux. Nat. Commun. **13**, 6597 (2022)

60.   Y. Chen et al., Observation of topological p-orbital disclination states in non-euclidean acoustic metamaterials. Phys. Rev. Lett. **129**, 154301 (2022)